Monthly Notices
of the
ROYAL ASTRONOMICAL SOCIETY

Mon. Not. R. Astron. Soc. **421,** 2798–2808 (2012) doi:10.1111/j.1365-2966.2012.20483.x

PG 1018−047: the longest period subdwarf B binary

J. Deca,[1⋆] T. R. Marsh,[2] R. H. Østensen,[3] L. Morales-Rueda,[4] C. M. Copperwheat,[2] R. A. Wade,[5] M. A. Stark,[6] P. F. L. Maxted,[7] G. Nelemans[8] and U. Heber[9]

[1]*Centrum voor Plasma-Astrofysica, Katholieke Universiteit Leuven, Celestijnenlaan 200B, B-3001 Leuven, Belgium*
[2]*Department of Physics, University of Warwick, Coventry CV4 7AL*
[3]*Instituut voor Sterrenkunde, Katholieke Universiteit Leuven, Celestijnenlaan 200D, B-3001 Leuven, Belgium*
[4]*Symetrica Security Ltd., Phi House, Enterprise Road, Southampton Science Park, Southampton SO16 7NS*
[5]*Department of Astronomy and Astrophysics, Pennsylvania State University, University Park, PA 16802, USA*
[6]*Department of Computer Science, Engineering and Physics, The University of Michigan-Flint, 303 E. Kearsley Street, Flint, MI 48502 , USA*
[7]*Astrophysics Group, Keele University, Keele, Staffordshire ST5 5BG*
[8]*Department of Astrophysics, IMAPP, Radboud University Nijmegen, PO Box 9010, 6500 GL Nijmegen, the Netherlands*
[9]*Dr Karl Remeis-Observatory & ECAP, Astronomical Institute, Friedrich-Alexander University Erlangen-Nuremberg, Sternwartstr. 7, 96049 Bamberg, Germany*

Accepted 2012 January 3. Received 2012 January 2; in original form 2011 November 14

ABSTRACT

About 50 per cent of all known hot subdwarf B stars (sdBs) reside in close (short-period) binaries, for which common-envelope ejection is the most likely formation mechanism. However, Han et al. predict that the majority of sdBs should form through stable mass transfer leading to long-period binaries. Determining orbital periods for these systems is challenging and while the orbital periods of ∼100 short-period systems have been measured, there are no periods measured above 30 d. As part of a large programme to characterize the orbital periods of sdB binaries and their formation history, we have found that PG 1018−047 has an orbital period of 759.8 ± 5.8 d, easily making it the longest period ever detected for a sdB binary. Exploiting the Balmer lines of the subdwarf primary and the narrow absorption lines of the companion present in the spectra, we derive the radial velocity amplitudes of both stars, and estimate the mass ratio $M_{\rm MS}/M_{\rm sdB} = 1.6 \pm 0.2$. From the combination of visual and infrared photometry, the spectral type of the companion star is determined to be mid-K.

Key words: binaries: close – binaries: spectroscopic – stars: evolution – stars: individual: PG 1018−047 – subdwarfs.

1 INTRODUCTION

Subdwarf B stars (sdBs) are core-helium burning stars with thin hydrogen envelopes. They are situated between the main sequence (MS) and the white dwarf cooling track at the blueward extension of the horizontal branch, the so-called extreme or extended horizontal branch (Heber et al. 1984; Heber 1986; Saffer et al. 1994). Subdwarf B stars have colours and spectral characteristics corresponding to those of a B star, but the Balmer lines are abnormally broad for the colour compared with Population I MS B stars due to their high surface gravity ($\log g \simeq 5.0$–6.0). Subdwarf B stars have a typical mass of $0.5\,{\rm M}_{\odot}$ (Heber et al. 1984) and can be found in all galactic populations. They are thought to be the dominant source for the ultraviolet (UV) upturn in early-type galaxies (Ferguson et al. 1991; Brown et al. 2000). A fraction of sdBs pulsate (Charpinet et al. 1996; Kilkenny et al. 1997), giving great opportunities to derive fundamental parameters (e.g. the stellar mass) and study their internal structure in detail (Green et al. 2003; Fontaine et al. 2008; Østensen 2009, 2010). Subdwarf B stars are also suggested to be very useful as age indicators using evolutionary population synthesis (Brown et al. 1997), or as distance indicators (Kilkenny et al. 1999). Since a large fraction of sdBs are members of binary systems (Maxted et al. 2001) and because they are intrinsically bright and ubiquitous, they are therefore an ideal population in which to study binary star evolution. For a comprehensive review on hot sdBs, we refer the reader to Heber (2009).

Han et al. (2003) describe in detail the formation and evolution of sdBs by using binary population synthesis models. They find that sdBs form via five main evolutionary channels: the first and second common-envelope channels, the first and second stable Roche lobe overflow (RLOF) channels and the helium white dwarf merger channel. This last channel is the only one that results in the formation of single sdBs. They find that the contribution of the second RLOF channel is not significant, leaving only three channels to form sdB binaries. Each of these three binary formation channels predicts a different orbital period distribution for the population of sdBs. The binaries formed through the first common-envelope channel should

⋆E-mail: jan.deca@wis.kuleuven.be

display orbital periods between 0.5 and ∼40 d and the companions to the sdBs will be MS stars. Binaries formed via the second common-envelope channel are expected to have white dwarf companions and their range of orbital periods will be wider, extending further into the short periods but not to long periods. Note as well that these common-envelope phases are not very well understood. Nelemans et al. (2000) have concluded from the observed double white dwarf population that its outcome may not always be a strong reduction of the orbital separation. Finally, sdB binaries formed through the first stable RLOF channel will have MS companions and will display orbital periods between 0.5 and ∼2000 d.

Han et al. (2003) conclude that their set 2 of simulations is the model that best describes the observed sample of short-period sdB binaries (Morales-Rueda et al. 2003). In this particular model (and also in nine out of the 12 models they describe), the majority of sdB binaries, between 60 and 70 per cent of the total, are formed via the first stable RLOF channel. At the same time, this is the channel most affected by observational selection effects decreasing the number of observable sdB binaries formed through this channel. These observational effects are primarily that sdBs with companions that are brighter than the sdB itself will not be identified as sdBs at all. The second effect has to do with observational limitations: it is easier to detect radial velocity (RV) variations from a short orbital period system than from a long one, as these are smaller and take longer to determine in the second case.

Despite extensive observational work, not a single system has been found in this long-period regime (first stable RLOF channel), whereas at present ∼100 sdB binaries with short periods are confirmed (Copperwheat et al. 2011; Geier et al. 2011). The orbital periods are mostly below 1 d, with a median period of 0.61 d. However, in this work, we will report on PG 1018−047, the first truly-long-period sdB binary. While this may be the product of binary evolution as suggested by the Han et al. (2002, 2003) models, we will find that it could also be the remnant of a hierarchical triple, as recently outlined by Clausen & Wade (2011).

Our target, PG 1018−047, has an apparent visual (Strömgren) magnitude $m_y = 13.32$ and was discovered as an UV-excess stellar object in the Palomar–Green Survey (Green, Schmidt & Liebert 1986). It was subsequently observed by Maxted et al. (2001) to check for RV variations. Although weak spectral features from a late-type companion are visible in the spectrum, Maxted et al. (2001) did not find any significant RV shifts using their variability criteria. This led to the conclusion that PG 1018−047 is probably not a binary with a short orbital period. The presence of the companion in the spectrum prompted continued follow-up of the system in order to determine how such a binary could have formed in the first place. We present the results after more than a decade of monitoring.

2 OBSERVATIONS AND REDUCTION

We have observed PG 1018−047 spectroscopically with several different instrument setups over a period of 10 yr. In Table 1, we summarize the observing dates, the setup used in each case, the wavelength range covered and the number of spectra obtained during each epoch. The data were obtained using the Isaac Newton Telescope (INT), William Herschel Telescope (WHT)[1] and Nordic Optical Telescope (NOT) on the island of La Palma, the Radcliffe telescope at the South African Astronomical Observatory (SAAO) and the Hobby–Eberly Telescope (HET) located at the McDonald Observatory in Texas. The different instrument setups were as follows:

For the *INT-R*ed spectra, the Intermediate Dispersion Spectrograph (IDS) was used. It is a long-slit spectrograph mounted on the Cassegrain Focal Station of the INT. The 500-mm camera together with the high-resolution *R*1200*R* grating and a windowed Tek5 CCD centred in $\lambda = 6560$ Å covered the Hα region. A 1-arcsec slit was used.

*INT-B*lue. The INT with the IDS, equipped with the 235-mm camera, the *R*1200*B* grating and a windowed EEV10 CCD were used to obtain these blue spectra. The 2002–2007 and 2008–2009 spectra were centred on, respectively, $\lambda = 4348$ and 4505 Å, covering as many Balmer lines to the blue as possible, including Hβ at 4861.327 Å. For all exposures, a 1-arcsec slit was used.

The *SAAO* data were obtained using the Radcliffe 1.9-m telescope together with the grating spectrograph plus the SITe back-illuminated CCD. Grating 4, with 1200 grooves mm^{-1} was used to obtain spectra covering Hγ and Hβ with a dispersion of 0.5 Å pixel^{-1} and a resolution of 1 Å at 4600 Å. The slit width varied from 1.2 to 1.5 arcsec depending on the seeing.

*WHT-R*ed. The WHT was equipped with the double arm Intermediate dispersion Spectrograph and Imaging System (ISIS). The *R*1200*R* grating and the Red+CCD were used to obtain the red spectra centred on $\lambda = 6560$ Å (2007 data) and $\lambda = 6521$ Å (2009 data). A slit width of 1.2 arcsec was used for the 2007 observations and a 1-arcsec slit for the 2009 ones.

The setup *WHT-B*lue denotes WHT data obtained using the ISIS with the *R*600*B* grating and the blue EEV10. The grating was centred on $\lambda = 4388$ Å with a 1-arcsec slit (2006 observations), on $\lambda = 4500$ Å with a 1.5-arcsec slit (2007 data), $\lambda = 4339$ Å with a slit width of 0.62 arcsec (2008) and on $\lambda = 4349$ Å with a 1.04-arcsec slit during the 2009 observations.

The *NOT* data were taken using the 2.56-m NOT. The FIbre-fed Echelle Spectrograph (FIES) highest resolution fibre (the 1.3-arcsec fibre offering a spectral resolution of $R = 67\,000$) covered the entire spectral range 3700–7300 Å without gaps in a single fixed setting.

The final setup, *HET*, refers to data from the bench-mounted high-resolution FIES, mounted on the 9.2-m HET operated in its $R = 15\,000$ resolution mode. In the '2 × 3' on-chip binning mode that was used, the dispersion was about 6 km s^{-1} per binned output pixel. A 2-arcsec optical fibre was used for the stellar target, and two additional fibers were used to record the sky spectrum. A cross-dispersing grating with 600 grooves mm^{-1} was used, centring $\lambda \approx 5822$ Å at the boundary between the 'blue' and 'red' CCDs. The useful wavelength coverage extended from 4810 to 6760 Å.

To reduce the spectra from the INT, WHT and SAAO, standard Starlink routines were used. Flat-fields were taken to correct for the pixel-to-pixel variations in the CCD and the bias correction was carried out by using the overscan region in each CCD frame. The objects were extracted with the optimal extraction algorithm of Marsh (1989). CuAr+CuNe arc spectra were taken before and after each target spectrum or after each set of two spectra at the target's position to calibrate these in wavelength. Fourth-order polynomials were computed to fit the lines in the arcs and the solutions were used for the calibration of the corresponding spectra.

The NOT data were reduced with the automatic data reduction software package FIESTOOL,[2] which makes use of the IRAF and

[1] Both the INT and WHT belong to the Isaac Newton Group of Telescopes (ING).

[2] Developed by Eric Stempels (http://www.not.iac.es/instru-ments/fies/fiestool/FIEStool.html)

Table 1. Journal of observations. Observers: P. F. L. Maxted (PFLM), T. Augustijn (TA), T. R. Marsh (TRM), Luisa Morales-Rueda (LM), G. Nelemans (GN), C. Copperwheat (CC), R. A. Wade (RAW) and M. A. Stark (MAS).

Date	Setup	λ region	Number of spectra	Mean dispersion (Å pixel^{-1})	Observer(s)
11–19/04/00	INT-R	Hα	4	0.39	PFLM
8–13/03/01	INT-R	Hα	11	0.39	PFLM
1–7/05/01	INT-R	Hα	9	0.39	PFLM
26–30/03/02	SAAO	Blue	6	0.49	TRM
25–27/04/02	INT-B	Blue	6	0.48	TA and TRM
9–16/04/03	INT-B	Blue	27	0.48	TRM
30/03–05/04/04	SAAO	Blue	5	0.49	LM
23–24/06/05	SAAO	Blue	2	0.50	LM
06/02/06	WHT-R	Hα	2	0.22	GN
	WHT-B	Blue	2	0.44	GN
09/03/07	WHT-B	Blue	4	0.44	Service
27/03–07/04/07	INT-B	Blue	11	0.48	TRM
29–31/03/07	WHT-R	Hα	5	0.25	GN
	WHT-B	Blue	5	0.44	GN
21–22/03/08	INT-B	Blue	4	0.48	CC
01/05/08	WHT-R	Hα	2	0.49	PFLM
	WHT-B	Blue	2	0.44	PFLM
11/03/09	INT-B	Blue	2	0.48	CC
30/04/09	WHT-R	Hα	4	0.25	TRM
	WHT-B	Blue	4	0.44	TRM
03/04/10	NOT	Hα + Blue	1	0.03	Service
06/12/07–23/03/10	HET	Hα + Blue	7	0.12	RAW and MAS

NumArray packages via a Python interface. After pre-processing, the raw frames were debiased and subsequently divided by a 2D normalized flat-field, correcting for the shape of each spectral order. Next the science spectra were extracted using the optimal extraction algorithm from Horne (1986) and corrected for the blaze shape. The wavelength calibration was done from a ThAr-lamp spectrum taken right before the science data. For the HET spectra we used standard IRAF tasks, organized using 'pipeline' scripts, to process the images and extract the spectra. Observations of PG 1018−047 were taken as pairs of 750-s exposures. Each pair was combined within IRAF, using the 'crreject' option in the task 'imcombine' to reduce cosmic-ray contamination; additional rejection of cosmic-ray artefacts was done later by hand. As a result of this observational effort, we have a total of 125 spectra of PG 1018−047.

3 RESULTS

3.1 The optical spectrum of PG 1018−047

The normalized optical spectrum of PG 1018−047 is shown in Fig. 1. It is obtained by averaging over a number of the ING/SAAO spectra taken at the same orbital phase, calculated using our best orbital solution from Section 3.2. In order to normalize the spectra, we fitted third-order polynomials to the regions free from absorption lines and divided the spectra by these fits. The mean spectrum shows several metal lines in the region between Hβ and Hγ. However, the He I line at 4472 Å, which is typical of sdBs, is absent. Instead, the Si III triplet (4553, 4568, 4575 Å) is the strongest feature. Several lines in the region between 4600 and 4700 Å can be identified with O II lines and possibly also N II. We made a fit to the mean spectrum of PG 1018−047 using the local thermodynamic equilibrium model grids of Heber, Reid & Werner (2000), with explicit metals of solar composition and abundances depleted by 0.0, 0.5, 1.0, 1.5 and 2.0 dex relative to solar. A reasonable fit is achieved with $T_{\rm eff} = 30\,500 \pm 200$ K, $\log g = 5.50 \pm 0.02$, and with the N and O abundance 1/10 of the solar value. In Fig. 1, a synthetic spectrum with these parameters broadened to match the resolution of the observed spectrum is shown. The model spectrum contains helium at a fraction $\log N({\rm He})/N({\rm H}) = -3.0$, but even this is clearly too much. In order to make helium fit with the observed spectrum, the model must be depleted to $\log N({\rm He})/N({\rm H}) < -4$. It is also clear that the abundances of the various elements are quite far from solar composition relative to each other, which is not unusual for the sdBs (Heber et al. 2000). Note that the K-star contributes some light also in the blue part of the spectrum, but insufficient to make any lines clearly visible in the spectrum. However, the contribution to the continuum might still be sufficient to affect the fitting procedure. In the Hα region, however, metal lines from the K star are clearly seen. Our high signal-to-noise ratio (S/N) mean spectrum has too low resolution to reliably infer the abundances of the individual components, and our high-resolution spectra have insufficient S/N.

3.2 The orbit of PG 1018−047

3.2.1 RV measurements

The RVs of the INT, WHT, SAAO and NOT spectra were determined following the procedure described by Morales-Rueda et al. (2003), that is, least-squares fitting of a line-profile model. This line-profile model was built up from three Gaussians per Balmer line with different widths and depths, but with a common central wavelength position which varies between the spectra. The parameters of the Gaussians were optimized by comparing the model to the normalized average spectrum over all observations [see Maxted et al. (2000c) for further details of this procedure]. For the blue spectra, we fit simultaneously for Hβ, Hγ and Hδ, whereas for the red spectra only the Hα line can be fitted. The RV of the NOT spectrum was determined using a model containing Hα, Hβ and

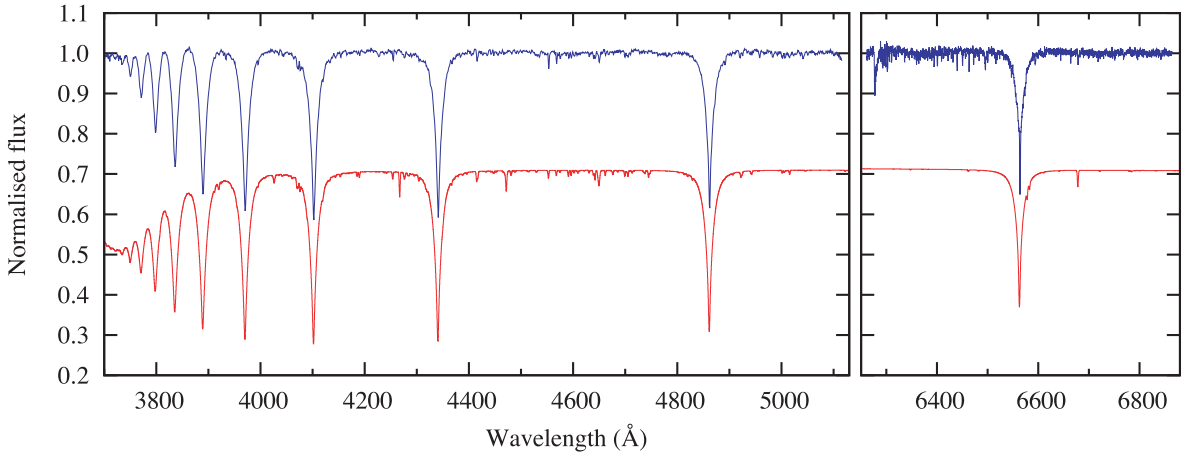

Figure 1. The mean spectrum of PG 1018−047 for the region covering Hβ to Hι (left-hand panel) and the region around Hα (right-hand panel). Plotted below the mean spectrum (shifted down for clarity) is a model spectrum for an sdB star (see text for details). Lines from the K dwarf are clearly seen in the red part, but the lines in the blue are from the sdB.

Table 2. Narrow absorption lines present in the optical spectrum (Fig. 1). The identification was done using the mid- and high-resolution spectral libraries of Montes et al. (1997) and also Ralchenko et al. (2010). The lines with an * were included in the template to determine the RVs of the secondary (see Section 3.2.3). For reference, we have added the wavelengths for the Balmer lines we adopted in our analysis as well.

λ (Å)	Element	λ (Å)	Element	λ (Å)	Element	λ (Å)	Element
4153.30	O II	4596.17	O II	6337.28*		6609.05*	
4164.79	Fe III, blend	4630.54	N II	6359.45*		6614.42*	
4189.80	O II	4639.70	O II, blend	6363.71*		6637.09*	
4253.59	S III + O II	4642.26	O II, N II	6394.45*		6644.39*	
4276.74	O II, blend	4649.14	O II	6400.43*		6664.37*	
4414.91	O II	4661.04	O II	6408.96*		6678.97*	
4416.58	O II	4676.23	O II	6412.37*			
4442.49	O II	4700.31	O II, blend	6422.05*		4101.735	Hδ
4552.65	Si III	4705.44	O II	6431.44*		4340.465	Hγ
4567.87	Si III	4710.04	O II	6439.70*		4861.327	Hβ
4574.78	Si III			6450.51*		6562.800	Hα
4590.57	O II	6335.83*		6456.49*			

Hγ (see also Table 2). The RVs from the seven HET spectra are obtained from the Hβ absorption line using simple Gaussian fitting to the core of the line within the IRAF 'splot' task. A list of the RVs and the uncertainties measured is given in Table 3.

3.2.2 Orbital parameters

Once the RVs for all spectra were known, we used the floating-mean periodogram (Cumming, Marcy & Butler 1999), a generalization of the well-known Lomb–Scargle periodogram (Lomb 1976; Scargle 1982), to determine the most probable frequencies (periods) present in the data. The method consists in fitting the RV data with a model composed of a sinusoid plus a constant of the form

$$v = \gamma + K \sin[2\pi f(t - t_0)], \quad (1)$$

with f the frequency and t the time of observation. This means we assume the binary system to have a circular orbit with semi-amplitude K and a systemic velocity γ. For each frequency ($f = 1/P$) we perform least-squares fitting of the data, solving for γ and K simultaneously using singular value decomposition (Press et al. 2002). In this way, we can obtain the χ^2 statistic of the model as a function of frequency, or in other words the periodogram.

In our initial period determination, the χ^2 values turned out larger than expected, given the number of data points, indicating that there must have been an extra unaccounted source of uncertainty, most likely due to systemic effects, intrinsic variability of the star or slit-filling errors (see also Morales-Rueda et al. 2003). Such errors are unlikely to be correlated with either the orbit or the statistical errors we have estimated. To allow for this we compute the level of systematic uncertainty (σ) per telescope which when added in quadrature to our error estimates gives a reduced $\chi^2 \approx 1$ for each of the INT and WHT subsets, telescope by telescope, relative to the preliminary fit. We increased the errors by $\sigma_{\rm INT} = 2.15\,{\rm km\,s^{-1}}$ and $\sigma_{\rm WHT} = 3.4\,{\rm km\,s^{-1}}$ for, respectively, the INT and WHT data. The formal NOT and HET errors were left unchanged since these are fibre-fed instruments which do not suffer from normal slit-guiding errors. Also the nine SAAO RVs were left as they were. Secondly, we used the average residual from each data set to our best orbital fit at that point to apply offsets to the INT, WHT and SAAO data sets[3] (respectively, 0.85, −2.00 and 4.63 km s^{-1}, predicted minus observed). Finally, we scale the errors of the entire data set

[3] Table A1 presents the RVs at this stage.

Table 3. The 125 RV measurements for PG 1018−047 with their formal errors from the least-squares fitting routine.

HJD −245 0000	RV (km s^{-1})	HJD −245 0000	RV (km s^{-1})	HJD −245 0000	RV (km s^{-1})
1646.471 35	31.3 ± 4.4	2741.527 95	49.8 ± 3.0	4189.547 10	52.1 ± 1.4
1646.476 50	20.5 ± 4.3	2741.539 09	53.3 ± 3.1	4189.547 12	42.9 ± 1.0
1654.460 74	24.7 ± 3.8	2741.548 57	48.8 ± 3.4	4190.409 80	51.9 ± 1.0
1654.467 80	32.1 ± 3.7	2741.558 07	48.2 ± 4.3	4190.409 82	46.0 ± 0.7
1977.482 20	49.6 ± 5.3	2743.420 40	50.4 ± 4.5	4190.424 20	53.5 ± 1.0
1978.625 33	55.2 ± 3.8	2743.434 51	60.3 ± 4.5	4190.424 22	50.7 ± 0.7
1979.540 44	45.0 ± 3.2	2743.521 28	52.2 ± 6.3	4191.596 77	52.1 ± 1.4
1979.599 58	65.5 ± 3.3	2744.358 95	54.3 ± 3.5	4191.596 77	44.1 ± 1.0
1979.606 55	54.0 ± 3.3	2744.373 08	49.7 ± 2.8	4193.371 92	51.4 ± 7.8
1982.514 89	52.2 ± 3.9	2744.391 86	49.4 ± 2.8	4195.357 18	41.6 ± 1.9
1982.521 85	54.6 ± 4.1	2744.405 98	51.4 ± 2.7	4195.371 21	36.4 ± 1.7
1982.554 21	57.8 ± 4.0	2744.425 29	53.9 ± 2.6	4195.614 47[c]	35.5 ± 2.5
1982.561 18	52.6 ± 3.9	2744.439 41	52.2 ± 2.6	4195.624 57[c]	38.1 ± 4.5
1982.600 59	57.5 ± 3.9	2745.379 82	48.8 ± 3.5	4197.514 56	43.8 ± 1.8
1982.607 55	53.2 ± 4.0	2745.393 94	45.3 ± 3.1	4197.528 58	43.6 ± 1.9
2031.367 69	62.1 ± 8.3	2745.409 87	51.4 ± 2.8	4441.008 11	39.7 ± 2.0
2031.374 66	41.4 ± 8.4	2745.423 99	51.9 ± 2.7	4469.931 58	36.0 ± 2.0
2031.386 41	49.5 ± 4.4	2746.441 31	54.6 ± 2.5	4502.850 94	33.5 ± 2.0
2032.482 43	54.9 ± 3.0	2746.455 44	51.0 ± 2.5	4547.378 72	33.0 ± 1.7
2032.496 33	53.6 ± 3.5	2746.474 12	55.4 ± 2.2	4547.406 65	31.1 ± 1.6
2033.396 72	53.8 ± 4.1	2746.488 24	44.8 ± 2.3	4547.621 44	29.6 ± 2.0
2033.403 69	53.8 ± 4.3	3095.382 27	26.8 ± 6.7	4547.648 44	32.4 ± 2.2
2037.455 84	54.1 ± 3.8	3095.403 36	19.0 ± 6.6	4550.714 05	26.7 ± 2.0
2037.462 82	50.9 ± 3.5	3098.337 04	12.9 ± 9.8	4562.688 46	29.6 ± 2.0
2360.366 83[a]	−33.8 ± 25.0	3101.318 90	18.8 ± 9.2	4588.351 23	29.7 ± 2.5
2360.377 45[a]	−4.6 ± 22.9	3101.329 56	19.7 ± 8.7	4588.351 25[d]	34.2 ± 2.6
2362.366 41[a]	17.5 ± 19.3	3545.219 53	51.4 ± 7.2	4588.356 46[d]	22.8 ± 2.6
2362.380 49[a]	5.4 ± 20.3	3546.207 56	52.6 ± 5.8	4588.356 48	29.5 ± 2.4
2364.392 75	23.1 ± 6.0	3772.554 66	35.6 ± 0.8	4902.423 20	34.8 ± 4.5
2364.403 38	17.9 ± 6.7	3772.554 67	26.7 ± 1.2	4902.444 18	36.6 ± 4.9
2390.511 13	34.6 ± 17.1	3772.685 64[b]	15.3 ± 0.9	4952.383 60	55.2 ± 2.8
2390.521 79	32.8 ± 9.0	3772.685 65	34.6 ± 1.4	4952.383 59	54.3 ± 5.1
2391.372 70	30.1 ± 4.3	4169.432 14	43.8 ± 1.2	4952.397 61	53.6 ± 3.9
2391.383 37	32.7 ± 3.6	4169.442 90	47.3 ± 1.4	4952.397 62	49.6 ± 2.2
2392.365 80	28.3 ± 2.1	4169.457 04	56.5 ± 2.0	4952.414 00	58.4 ± 1.8
2392.379 93	24.5 ± 2.0	4169.467 74	52.6 ± 6.1	4952.414 01	51.8 ± 2.9
2739.510 74	45.0 ± 3.6	4186.547 93	38.0 ± 3.6	4952.428 02	51.1 ± 2.3
2739.520 29	46.7 ± 3.8	4186.558 10	40.1 ± 11.8	4952.428 02	58.4 ± 1.5
2740.445 14	49.8 ± 3.2	4188.419 25	39.9 ± 3.0	5202.927 61	36.5 ± 2.0
2740.454 65	51.9 ± 3.0	4188.433 28	42.1 ± 2.9	5278.716 93	32.8 ± 2.0
2741.508 96	49.7 ± 3.1	4189.536 08	49.9 ± 1.5	5295.960 94	35.0 ±1.6
2741.518 46	49.4 ± 3.1	4189.536 09	42.6 ± 1.0		

[a]The SAAO science frames belonging to these four RVs were made with very marginal observing conditions. The resulting unreliable RVs are therefore not considered in the remaining analysis.
[b]This is a discrepant WHT data point, taken during service observations in 2006. It is not in line with the other data taken on the same night and therefore given no weight in the remaining analysis.
[c]For the blue WHT science frames belonging to these two RVs, only a single arc frame was available, taken before the first of the two subsequent observations.
[d]These two WHT observations in the Hβ–Hδ region had no flat-fields or bias frames available.

multiplicatively by a factor 1.244 to obtain a χ^2 value equal to the degrees of freedom (d.o.f.).

Fig. 2 shows the resulting RV periodogram for PG 1018−047 in the region where we find the lowest χ^2 values. The best solution is found around 760 d, followed by a group of 1 d aliases and the yearly aliases of the long period around 250 d. An overview of the best aliases with their corresponding χ^2 values is given in Table 4. Given the large inhomogeneity of the data sets, we realize that the treatment of the errors described above might not be perfect in all details. Therefore, we have considered alternative methods to weight the data and errors as well, but the essential result, the long period, was unchanged throughout.

In Table 4, we also quote the mass functions of the companion, calculated using

$$f_{\rm m} = \frac{M_{\rm MS}^3 \sin^3 i}{(M_{\rm sdB} + M_{\rm MS})^2} = \frac{P K_{\rm sdB}^3}{2\pi G}. \quad (2)$$

The minimum mass of the companion, assuming a typical sdB mass of 0.5 $M_\odot$ (Heber et al. 1984), is also given in each case. These numbers will be used later to constrain the nature of the companion

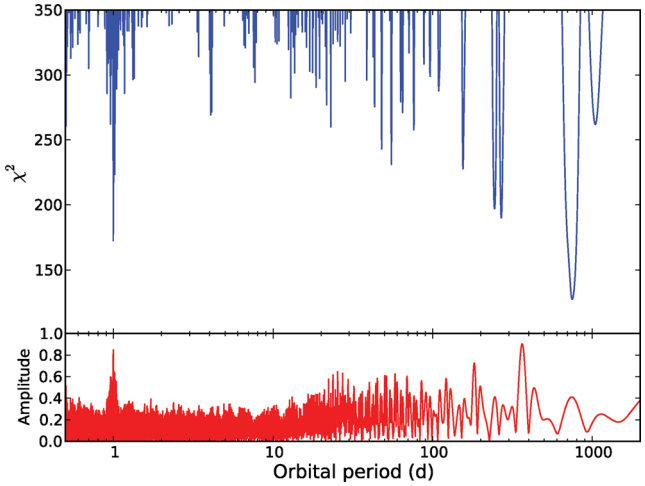

Figure 2. The RV periodogram for PG 1018−047, showing the most probable orbital periods present in the data. The lower panel shows the spectral window.

Table 4. The best orbital periods found from the RV periodogram for PG 1018−047. The χ^2 value, mass function and the minimum mass of the companion obtained by assuming an sdB mass of 0.5 $M_\odot$ are also given.

Alias	Period (d)	χ^2	f_m ($M_\odot$)	M_{2min} ($M_\odot$)
1	759.80	117	0.172 45	0.589 27
2	0.9987	188	0.000 18	0.037 04
3	241.35	238	0.026 02	0.243 13
4	267.93	258	0.055 82	0.340 31
5	1.0184	259	0.000 13	0.033 32

Table 5. The best orbital solution for PG 1018−047 assuming a circular and eccentric orbit.

	Circular	Eccentric
P_{orb} (d)	759.8 ± 5.8	755.9 ± 5.1
γ (km s^{-1})	38.2 ± 0.5	38.0 ± 0.9
e	0	0.246 ± 0.052
ω (°)		0 ± 24
HJD_0 (d)	$2453\,335.0 \pm 10.5$	$2453\,343.0 \pm 14.7$
K_{sdB} (km s^{-1})	13.0 ± 0.8	12.6 ± 0.8
K_{MS} (km s^{-1})	8.1 ± 1.0	

star and vice versa to show that our orbital solution is plausible, given the properties of the secondary.

Table 5 lists the orbital parameters for our best orbital solution found for PG 1018−047 and in Fig. 3 the RV curve folded on the period is shown.

3.2.3 *The secondary orbit*

Narrow metal lines of a cool companion were present in addition to the Balmer absorption lines from the sdB star, allowing us to obtain RV variations for the secondary star. The blue spectra did not contain enough signal from the companion to be useful, so we focused on the HET, NOT and red WHT/INT spectra. We determined the RVs of the secondary by means of cross-correlation with a template spectrum (Tonry & Davis 1979).

For the HET data we cross-correlated with 61 Cyg B (K7V), which was obtained as part of a different programme on 2010 April 15, using HRS in its $R = 30\,000$ mode with a 316 groove mm^{-1} cross disperser centred at 6948 Å. As a result only seven orders from the red CCD (six, on one night) were available for cross-correlation, covering 6000–6760 Å (orders containing Hα or strong telluric lines were excluded).

For the other data we constructed a template from our data using the average red spectrum of PG 1018−047 (the upper panel in Fig. 1). Every (by eye) recognizable absorption feature of the secondary was fitted with a Gaussian profile, similar to the method described in Section 3.2.1. All features possibly originating in the primary or of telluric origin were masked out, leaving a total of 19 lines from the cool companion in the template (see also Table 2).

Unfortunately, the quality of the secondary RVs obtained from the red INT and WHT spectra were not sufficient to derive any trustworthy orbital period from a periodogram or to estimate the orbital semi-amplitude K_{MS} for the secondary. We therefore used our best orbital period obtained from the primary RVs (Table 5) to phase-bin the 37 medium-resolution red spectra before the cross-correlation routine. In total, seven out of 40 bins are filled. The HET and NOT spectra were left unbinned.

In Fig. 4, we have plotted phase versus RV (see also Table 6). Using least-squares fitting, we estimated the projected semi-amplitude of the secondary to be $K_{MS} = 8.1 \pm 1.0$ km s^{-1}, which constrains the mass ratio of the secondary to the primary star to be $q = M_{MS}/M_{sdB} = 1.6 \pm 0.2$. The χ^2 value of the fit was 13.29, given 15 data points minus two fitting parameters.

3.2.4 *Eccentricity of the orbit*

In Sections 3.2.2 and 3.2.3, the analysis was based upon the assumption that PG 1018−047 has a circular orbit. However, we also tried fitting eccentric orbits using the Markov chain Monte Carlo method (Gilks, Richardson & Spiegelhalter 1995) obtaining an eccentricity of 0.246 ± 0.052; the favoured period for these fits decreased from 759.8 ± 5.7 to 755.9 ± 5.1 d and had $\chi^2 = 152$, starting from the RVs in Table A1. To obtain χ^2/d.o.f. $= 1$ we needed to scale the errors by a factor 1.153. Table 5 presents the orbital parameters. The argument of periapsis (ω) is defined as the angle in the orbital plane between the ascending node and the line of apsides. 0° indicates that the major-axis of the ellipse is in the plane of the sky. Note as well that HJD_0 is given as the ascending node passage minus $P_{orb}/4$ to be consistent with our definition for the circular orbit (see equation 1).

Computing the F-statistic, we tested whether eccentricity was needed in our model. Assuming a locally linear model, the variable $X = \chi^2_{circ} - \chi^2_{ecc}$ should itself have a χ^2 distribution with 2 d.o.f. (the eccentricity fit parameters), independent of the χ^2 of the 114 d.o.f. of the eccentric orbit.

$$F = \frac{\left(\chi^2_{circ} - \chi^2_{ecc}\right)/2}{\chi^2_{ecc}/114} = 11.24$$

should then be distributed as $F(2; 114)$ under the null hypothesis that the orbit is circular. The chances of such a large value are very small, meaning we reject the null hypothesis at the 99.9 per cent significance level in favour of an eccentric orbit. Although formally significant the heterogeneous nature of our data and the limited phase coverage lead us to be wary of claiming a definitive detection of eccentricity. However, it is equally true that the orbit could be significantly non-circular.

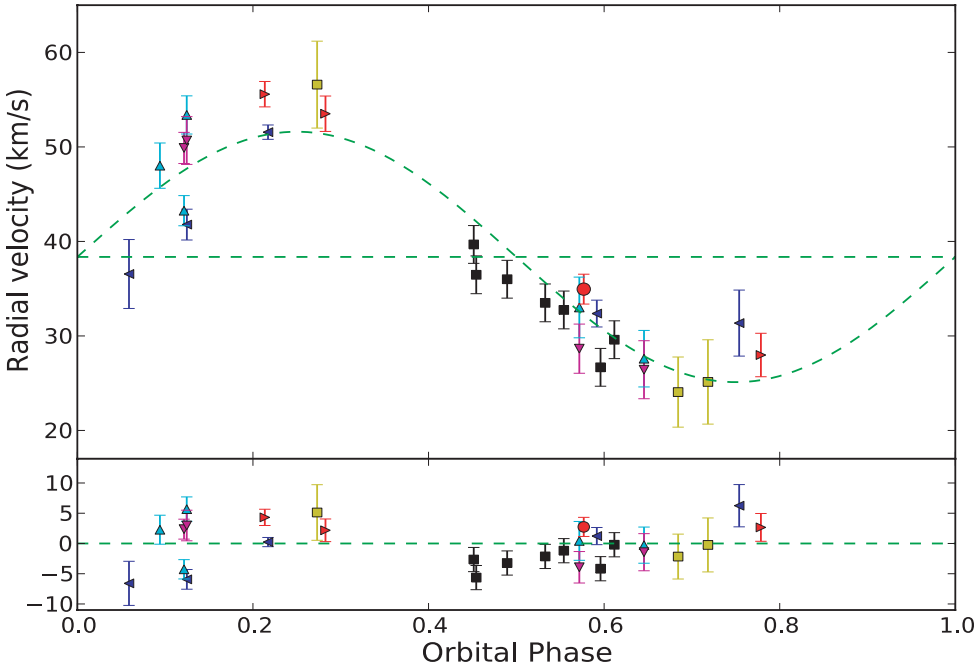

Figure 3. RV curve for the sdB component of PG 1018−047 assuming a circular orbit. We have averaged the RVs per observation run. The lower panel shows the residuals. The black squares are the seven RVs from the HET spectra, the red dot is the NOT/FIES data point, the yellow squares are the SAAO observations, the blue left-headed triangles and red right-headed triangles are, respectively, the blue and red INT data points, and the cyan up and magenta down triangles correspond to the blue and red WHT RVs. In the upper panel, the green-dashed straight line represents the systemic velocity (γ).

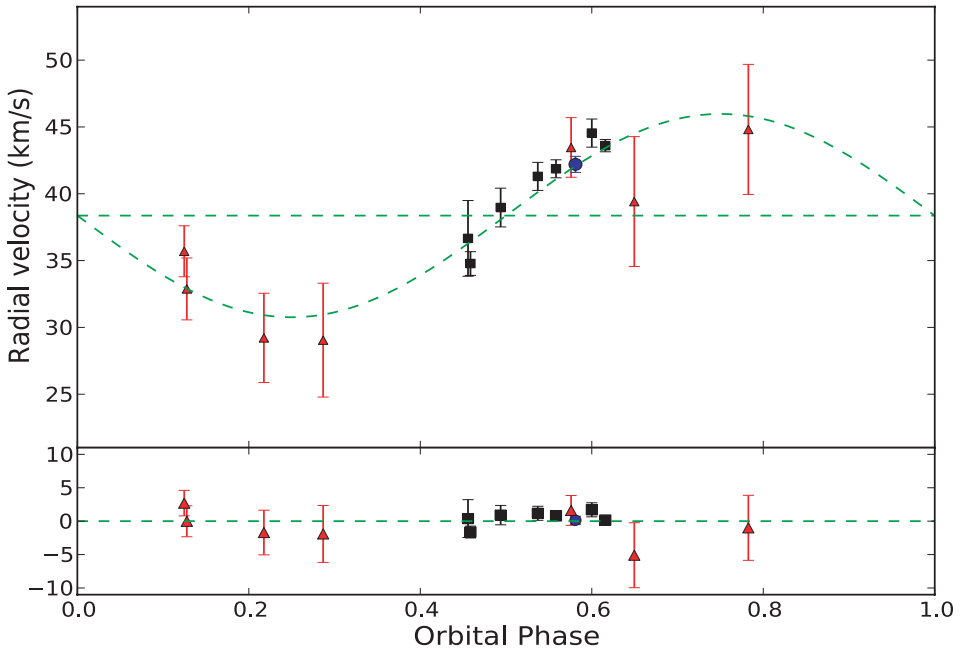

Figure 4. The orbital fit for the secondary star assuming a circular orbit. The red triangles are the RVs from the cool companion, obtained from the intermediate-resolution spectroscopy. The NOT measurement is plotted with a blue dot and the HET data with black squares. The RV curve (dashed green) is also shown.

3.3 The nature of the companion

We determined the spectral type of the companion star by minimizing the residuals after subtracting different template star spectra from the mean red PG 1018−047 spectrum in the wavelength region between 6390 and 6700 Å. We masked out Hα, because the line contains a large contribution from the sdB. This optimal subtraction routine (Marsh, Robinson & Wood 1994) is sensitive to both the rotational broadening $v_{\rm rot} \sin i$ and the fractional contribution f of the companion star to the total flux. We used template stars from two different origins in the spectral range F0–M9: Kurucz models (Munari et al. 2005, solar composition) and 43 real star templates (Montes et al. 1997). All templates were prepared so that they had the same wavelength coverage and resolution as our normalized PG 1018−047 spectrum in the Hα region.

Table 6. The RVs of the cool companion.

Bin	Number of spectra in the bin	Average phase	RV (km s^{-1})
0.100–0.125	Two	0.1247	35.7 ± 1.9
0.125–0.150	Seven	0.1277	32.9 ± 1.3
0.200–0.225	Eleven	0.2176	29.2 ± 3.3
0.250–0.275	Nine	0.2867	29.0 ± 4.3
0.4556	HET		36.7 ± 2.8
0.4585	HET		34.8 ± 0.9
0.4937	HET		39.0 ± 1.5
0.5370	HET		41.3 ± 1.1
0.5583	HET		41.9 ± 0.7
0.575–0.600	Two	0.5759	43.5 ± 2.2
0.5810	NOT		40.2 ± 0.6
0.6000	HET		44.5 ± 1.1
0.6158	HET		43.6 ± 0.6
0.625–0.650	Two	0.6496	39.4 ± 4.9
0.775–0.800	Four	0.7826	44.8 ± 4.9

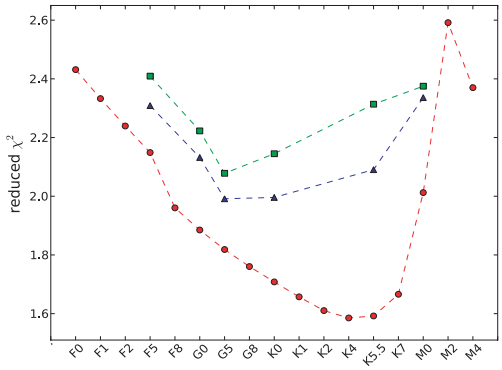

Figure 5. Results of the optimal subtraction routine for the Kurucz templates. The circles plot the results for dwarf stars, whereas the triangles and squares plot the reduced χ^2 versus spectral type for, respectively, subgiant and giant stars.

Fig. 5 clearly shows the difference in χ^2 between the dwarf and (sub)giant templates. The MS models, which have the lowest χ^2 values, show a distinct minimum at spectral type K4–K6, whereas the (sub)giant models seem to converge to a spectral type G5. This is consistent with the set of template spectra from Montes et al. (1997) as well, where we find the best χ^2 for the K5V star HD 201091 (61 Cyg A), followed by a K7V and a K3V star. For M stars the worst values are found. The best non-dwarf templates were both G5 stars.

Since PG 1018−047 was observed by 2MASS, we adopt a similar approach to Stark & Wade (2003) as a complementary way to identify the spectral type of the companion star. We choose to focus on $J - K_S$ versus $B - V$ and $J - K_S$ versus $V - K_S$ and convert the Strömgren magnitudes to the Johnson system following the approach of Turner (1990). The calculated colours are given in the lower part of Table 7.

The next step is to compare the PG 1018−047 colours to a theoretical grid of colours for sdB+MS binaries while varying the fraction of light at V, which arises from the companion. Defining this fraction as

$$f = \frac{F_{V_{\rm MS}}}{F_V} = \frac{F_{V_{\rm MS}}}{F_{V_{\rm sdB}} + F_{V_{\rm MS}}},$$

we find the combined colour (e.g. for $B - V$) from the expression

$$(B-V)_{\rm sdB+MS} = -2.5 \log\left[(1-f)10^{-(B-V)_{\rm sdB}/2.5} + f10^{-(B-V)_{\rm MS}/2.5}\right].$$

Table 7. Magnitudes and colours for PG 1018−047. The $B - V$ colour is calculated using the transformation formula from Turner (1990).

2MASS (infrared) (Skrutskie et al. 2006)		Strömgren (visual) (Wesemael et al 1992)	
J	= 13.298 (.026)	y	= 13.320 (.005)
H	= 12.980 (.027)	$b - y$	= −0.086 (.004)
K_S	= 12.928 (.033)	$u - b$	= −0.073 (.006)
		m_1	= 0.076 (.013)
Calculated colours			
$B-V$	= −0.20 (.007)		
$J-K_S$	= 0.370 (.042)		
$V-K_S$	= 0.392 (.038)		

Colour indices for late-type stars are taken from Johnson (1966). The typical colours for a single sdB are taken from Stark & Wade (2003).

Fig. 6 shows that as the fractional contribution f at V from the secondary increases, the $B - V$ index shifts to redder values. On the other hand, the cooler the companion becomes, the more the K_S band dominates the $J - K_S$ index. Swapping the $B - V$ index for the $V - K_S$ colour shows a similar trend. Zooming in on PG 1018−047, we find a spectral classification K3–K6, which is consistent with the results from the optimal subtraction routine. We estimate the contribution of the secondary to be 6.1 ± 1.0 per cent in the V band.

4 DISCUSSION

The role of the long-period binary system PG 1018−047 in refining our understanding of the origin and evolution of hot subdwarf stars depends on whether its present orbit is circular or eccentric.

4.1 Evolution assuming a circular orbit

If PG 1018−047 indeed has a circular orbit, one can assume that tidal interaction has occurred between the sdB and the dK5 star. This means that from a theoretical point of view PG 1018−047 might be an important system, as it becomes a good candidate for formation through the first stable RLOF channel described by Han et al. (2003). From fig. 15 in Han et al. (2003) we deduce that an sdB binary with a mid-K companion is feasible. However, these systems are all subgiants and giants evolved from B stars (i.e. more massive stars at a later evolutionary state). Also, to have stable RLOF on the first giant branch on to a companion that is only 0.6–0.7 $M_\odot$ and still to end up with such a long period, mass transfer would have to be close to conservative to avoid excessive angular momentum loss. If we want the mass donor to evolve in a Hubble time, it must have started with an initial mass of 0.8 $M_\odot$ or greater, meaning that the initial mass of the present K star must have been no more than ∼0.3–0.4 $M_\odot$. However, then the initial mass ratio $q_0 \gtrsim 2$ is not compatible with conservative mass transfer on the red giant branch, leading to a contradiction.

Secondly, we can consider the alternative common-envelope prescription from Nelemans et al. (2000). In Nelemans (2010), a population of sdB stars is simulated in which the first phase of mass transfer can be described by this alternative common-envelope prescription (Nelemans et al. 2001). Interestingly, in that model a substantial fraction of the sdB stars with low- and intermediate-mass MS companions have rather large orbital periods (100–1000 d, see their fig. 2) and the parameters of PG 1018−047 actually fall right in a densely populated area of the model. Thus, a sample of these

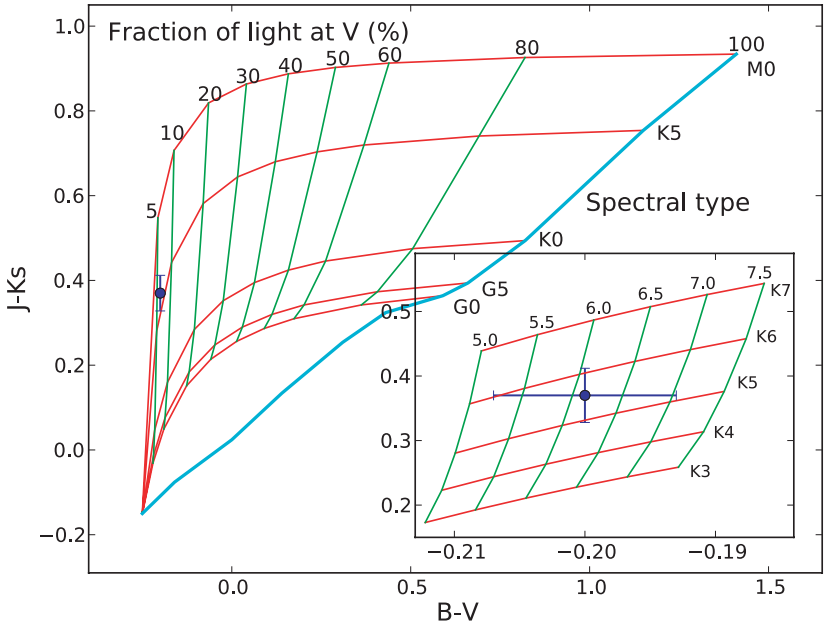

Figure 6. Grid of composite colours in $B - V$ versus $J - K_S$ space by combining the light from a typical hot subdwarf with that of a Population I MS star assuming various fractional contributions to the total light in the V band by the late-type star. The blue dot marks the values for PG 1018−047. A close-up is shown in the small inset figure. The diagonal cyan line indicates the location of the Population I MS.

long-period sdB binaries will give another way of testing the outcome of the common-envelope phase.

4.2 Evolution assuming an eccentric orbit

Clausen & Wade (2011) propose that binaries similar to PG 1018−047 can be remnants of original hierarchical triple systems, in which the inner binary has merged and evolved into the sdB star, and the outer (current sdB+MS) binary was never tidally interacting and is thus irrelevant to the production of the sdB. In the Han et al. (2002, 2003) merger scenario, two helium white dwarfs merge to make an object capable of core helium burning, and the resulting range of masses for the sdB star is 0.3–0.8 $M_\odot$. In the new formation channel proposed by Clausen & Wade (2011), a helium white dwarf merges with a low-mass hydrogen-burning star whose resultant total mass is ∼0.6 $M_\odot$. Depending on the mixing history, this object has either a pre-formed helium core or is helium-enriched throughout, and the star experiences a greatly accelerated evolution to the tip of the red giant branch. Only minimal loss is required to remove the residual hydrogen envelope from this object at the time of normal degenerate helium ignition, so the expected mass range for the sdB star in this channel is narrow and at the 'canonical value ∼0.5 $M_\odot$. There is ample room inside the ∼760 d orbit of the present-day PG 1018−047 binary system to accommodate an inner binary that underwent such evolution, and there is no cause for the outer orbit to have been circularized. The Clausen & Wade (2011) scenario could account for stars like PG 1018−047 with long (and possibly eccentric) binary orbits. Stable RLOF, on the other hand, predicts perfectly circular orbits.

5 CONCLUSIONS

With an orbital period of 759.8 ± 5.8 d, PG 1018−047 is the first long-period sdB+MS system for which a period has been determined. The spectral type of the companion was found to be a K5 dwarf star, consistent with the mass ratio $M_{\rm MS}/M_{\rm sdB} = 1.6 \pm 0.2$ derived from the RV amplitudes of both stars. However, one has to note that the stated numbers are only indicative of the true orbital parameters, since they are sensitive to the exact uncertainties assigned to the RV data and the assumption of a circular versus eccentric orbit.

At first sight, PG 1018−047 is a good candidate for formation through stable RLOF if the orbit can be demonstrated to be circular. The predicted number of sdB binaries formed through this channel amounts to the largest contribution of sdB binaries according to binary population synthesis calculations (Han et al. 2002, 2003). At the same time, the number of known binaries that have been confirmed as having formed through this channel is small/nil compared to those formed through the common-envelope channels. Alternatively, if the common envelope is governed by the Gamma formalism for the common envelope, as used in Nelemans (2010), there are a population of long-period post-common-envelope binaries with low-mass secondaries. Thus, observing more of these binaries can constrain the first phase of mass transfer.

If the orbit turns out to be eccentric, the present binary may instead be the remnant of a hierarchical triple-star progenitor system, as outlined by Clausen & Wade (2011). Further observations are needed to better establish the orbit of PG 1018−047.

ACKNOWLEDGMENTS

TRM and CMC were supported under a Science and Technology Facilities Council (STFC) rolling grant during the course of this work. RHØ has received funding from the European Research Council under the European Community's Seventh Framework Programme (FP7/2007–2013)/ERC grant agreement no. 227224 (PROSPERITY), as well as from the Research Council of K. U. Leuven grant agreement GOA/2008/04. LM was supported by a PPARC post-doctoral grant and by a NWO-VIDI grant 639.042.201 to P. J. Groot during this work. RAW and MAS gratefully acknowledge support from NSF grant AST-0908642. The INT and WHT are operated on the island of La Palma by the ING in the Spanish Observatorio del Roque de los Muchachos of the Instituto de Astrofísica

de Canarias. We thank PATT for their support of this programme. We also thank the ING service scheme for obtaining some of the data. This paper uses observations made at the SAAO. A portion of the data reported herein was obtained with the HET, which is a joint project of the University of Texas at Austin, the Pennsylvania State University, the Stanford University, Ludwig-Maximillians-Universität München and Georg-August-Universität Göttingen. The HET is named in honour of its principal benefactors, William P. Hobby and Robert E. Eberly. This paper also uses observations made with the NOT, operated on the island of La Palma jointly by Denmark, Finland, Iceland, Norway and Sweden, in the Spanish Observatorio del Roque de los Muchachos of the Instituto de Astrofísica de Canarias.

REFERENCES

Brown T. M., Ferguson H. C., Davidsen A. F., Dorman B., 1997, ApJ, 482, 685
Brown T. M., Bowers C. W., Kimble R. A., Sweigart A. V., Ferguson H. C., 2000, ApJ, 532, 308
Charpinet S., Fontaine G., Brassard P., Dorman P., 1996, ApJ, 471, L103
Clausen D., Wade R. A., 2011, ApJ, 733, L42
Copperwheat C. M., Morales-Rueda L., Marsh T. R., Maxted P. F. L., Heber U., 2011, MNRAS, 410, 1113
Cumming A., Marcy G. W., Butler R. P., 1999, ApJ, 526, 890
Ferguson H. C. et al., 1991, ApJ, 382, L69
Fontaine G., Brassard P., Charpinet S., Green E. M., Chayer P., Randall S. K., van Grootel V., 2008, in Heber U., Jeffery C. S., Napiwotzki R., eds, ASP Conf. Ser. Vol. 392, Hot Subdwarf Stars and Related Objects. Astron. Soc. Pac., San Francisco, p. 231
Geier S. et al., 2011, A&A, 530, A28
Gilks W. R., Richardson S., Spiegelhalter D., 1995, Markov Chain Monte Carlo in Practice. Chapman & Hall, London
Green E. M. et al., 2003, ApJ, 583, L31
Green R. F., Schmidt M., Liebert J., 1986, ApJS, 61, 305
Han Z., Podsiadlowski Ph., Maxted P. F. L., Marsh T. R., Ivanova N., 2002, MNRAS, 336, 449
Han Z., Podsiadlowski Ph., Maxted P. F. L., Marsh T. R., 2003, MNRAS, 341, 669
Heber U., 1986, A&A, 155, 33
Heber U., 2009, ARA&A, 47, 211
Heber U., Hunger K., Jonas G., Kudritzki R. P., 1984, A&A, 130, 119
Heber U., Reid I. N., Werner K., 2000, A&A, 363, 198
Horne K., 1986, PASP, 98, 609
Johnson H. L., 1966, ARA&A, 4, 193
Kilkenny D., Koen C., O'Donoghue D., Stobie R. S., 1997, MNRAS, 285, 640
Kilkenny D., Koen C., Jeffery J., Hill C. S., O'Donoghue D., 1999, MNRAS, 310, 1119
Lomb N. R., 1976, Ap&SS, 39, 447
Marsh T. R., 1989, PASP, 101, 1032
Marsh T. R., Robinson E. L., Wood J. H., 1994, MNRAS, 266, 137
Maxted P. F. L., Marsh T. R., Moran C. K. J., 2000, MNRAS, 319, 305
Maxted P. F. L., Heber U., Marsh T. R., North R. C., 2001, MNRAS, 326, 139
Montes D., Martín E. L., Fernandéz-Figueroa M. J., Cornide M., De Castro E., 1997, A&AS, 123, 473
Morales-Rueda L., Maxted P. F. L., Marsh T. R., North R. C., Heber U., 2003, MNRAS, 338, 752
Munari U., Sordo R., Castelli F. Zwitter T., 2005, A&A, 442, 1127
Nelemans G., 2010, Ap&SS, 329, 25
Nelemans G., Verbunt F., Yungelson L. R., Portegies Zwart S. F., 2000, A&A, 360, 1011
Nelemans G., Yungelson L. R., Portegies Zwart S. F., Verbunt F., 2001, A&A, 365, 491
Press W. H., Teukolsky S. A., Vetterling W. T., Flannery B. T., 2002, Numerical Recipes in C: The Art of Scientific Computing. Cambridge Univ. Press, Cambridge
Ralchenko Y., Kramida A. E., Reader J., NIST ASD Team, 2010, NIST Atomic Spectra Database (ver. 4.0.1). National Institute of Standards and Technology, Gaithersburg, MD (available at: http://physics.nist.gov/asd)
Saffer R. A., Bergeron P., Koester D., Liebert J., 1994, ApJ, 432, 351
Scargle J. D., 1982, ApJ, 263, 835
Skrutskie M. F. et al., 2006, AJ, 131, 1163
Stark M. A., Wade R. A., 2003, AJ, 126, 1455
Tonry J., Davis M., 1979, AJ, 84, 1511
Turner D. G., 1990, PASP, 102, 1331
Østensen R. H., 2009, Commun. Asteroseismol., 159, 75
Østensen R. H., 2010, Astron. Nachr., 331, 1026

APPENDIX A: RADIAL VELOCITY MEASUREMENTS WITH ERROR AND OFFSET CORRECTION

In Table A1, we report the RV values for PG 1018−047 with error and offset correction, as used for the final orbital fit results.

Table A1. RV measurements for PG 1018−047 with error and offset correction, as used for the final orbital fit results.

HJD (−245 0000)	RV ($km\,s^{-1}$)	HJD (−245 0000)	RV ($km\,s^{-1}$)	HJD (−245 0000)	RV ($km\,s^{-1}$)
INT-B		4197.528 58	44.4 ± 2.9	WHT-B	
($\sigma = 2.15\,km\,s^{-1}$, offset = $+0.85\,km\,s^{-1}$)		4547.378 72	33.9 ± 2.7	($\sigma = 3.40\,km\,s^{-1}$, offset = $-2.01\,km\,s^{-1}$)	
2390.511 13	35.5 ± 17.2	4547.406 65	32.0 ± 2.7	3772.554 66	33.5 ± 3.5
2390.521 79	33.6 ± 9.2	4547.621 44	30.4 ± 2.9	3772.685 65	32.5 ± 5.4
2391.372 70	31.0 ± 4.8	4547.648 44	33.2 ± 3.0	4169.432 14	41.8 ± 3.7
2391.383 37	33.6 ± 4.2	4902.423 20	35.7 ± 4.9	4169.442 90	45.2 ± 3.7
2392.365 80	29.2 ± 3.0	4902.444 18	37.5 ± 5.4	4169.457 04	54.5 ± 4.0
2392.379 93	25.3 ± 3.0	INT-R		4169.467 74	50.6 ± 7.0
2739.510 74	45.9 ± 4.2	($\sigma = 2.15\,km\,s^{-1}$, offset = $+0.85\,km\,s^{-1}$)		4189.536 09	40.5 ± 3.6
2739.520 29	47.5 ± 3.9	1646.471 35	32.1 ± 4.9	4189.547 112	40.9 ± 3.6
2740.445 14	50.6 ± 39	1646.476 50	21.3 ± 4.8	4190.409 82	44.0 ± 3.5
2740.454 65	52.7 ± 3.7	1654.460 74	25.6 ± 4.3	4190.424 22	48.7 ± 3.5
2741.508 96	50.5 ± 3.7	1654.467 80	32.9 ± 4.3	4191.596 77	42.1 ± 3.6
2741.518 46	50.3 ± 3.7	1977.482 20	50.4 ± 5.7	4588.351 23	27.7 ± 4.3
2741.527 95	50.6 ± 3.7	1978.625 33	56.0 ± 4.4	4588.356 48	27.5 ± 4.2
2741.539 09	54.2 ± 3.7	1979.540 44	50.8 ± 3.9	4952.383 60	53.1 ± 4.4
2741.548 57	49.7 ± 4.0	1979.599 58	66.3 ± 4.0	4952.397 63	47.6 ± 4.1
2741.558 07	49.0 ± 4.8	1979.606 55	54.8 ± 4.0	4952.413 40	56.4 ± 3.9
2743.420 40	51.3 ± 4.9	1982.514 89	53.0 ± 4.4	4952.428 02	56.4 ± 3.8
2743.434 51	61.1 ± 5.0	1982.521 85	55.5 ± 4.6	WHT-R	
2743.521 28	53.0 ± 6.6	1982.554 21	58.7 ± 4.5	($\sigma = 3.40\,km\,s^{-1}$, offset = $-2.01\,km\,s^{-1}$)	
2744.358 95	55.2 ± 4.1	1982.561 18	53.4 ± 4.4	3772.554 67	24.7 ± 3.6
2744.373 08	50.5 ± 3.6	1982.600 59	58.4 ± 4.4	4189.536 09	47.9 ± 3.8
2744.391 86	50.2 ± 3.5	1982.607 55	54.0 ± 4.5	4189.547 10	50.1 ± 3.7
2744.405 98	52.3 ± 3.5	2031.367 69	62.9 ± 8.6	4190.409 80	49.9 ± 3.6
2744.425 29	54.7 ± 3.3	2031.374 66	42.2 ± 8.7	4190.424 20	51.5 ± 3.6
2744.439 41	53.1 ± 3.3	2031.386 41	50.3 ± 4.9	4191.596 77	50.1 ± 3.7
2745.379 82	49.6 ± 4.1	2032.482 43	55.7 ± 3.7	4588.351 25	32.2 ± 4.4
2745.393 94	46.1 ± 3.7	2032.496 33	54.5 ± 4.1	4588.356 46	20.7 ± 4.3
2745.409 87	52.2 ± 3.5	2033.396 72	54.7 ± 4.6	4952.383 59	52.3 ± 6.2
2745.423 99	52.7 ± 3.4	2033.403 69	54.6 ± 4.8	4952.397 61	51.6 ± 5.2
2746.441 31	55.4 ± 3.3	2037.455 84	54.9 ± 4.4	4952.414 00	49.8 ± 4.5
2746.455 44	51.8 ± 3.3	2037.462 82	51.8 ± 4.1	4952.428 02	49.1 ± 4.1
2746.474 12	56.2 ± 3.1	SAAO		NOT	
2746.488 24	45.7 ± 3.2	($\sigma = 0\,km\,s^{-1}$, offset = $+4.63\,km\,s^{-1}$)		($\sigma = 0\,km\,s^{-1}$, offset = $0\,km\,s^{-1}$)	
4186.547 93	38.8 ± 4.2	2364.392 75	27.7 ± 6.0	5295.960 94	35.0 ± 1.58
4186.558 10	40.9 ± 12.0	2364.403 38	22.5 ± 6.6	HET	
4188.419 25	40.8 ± 3.6	3095.382 27	31.5 ± 6.6	($\sigma = 0\,km\,s^{-1}$, offset = $0\,km\,s^{-1}$)	
4188.433 28	42.9 ± 3.6	3095.403 36	23.6 ± 6.6	4441.008 11	39.68 ± 2.0
4193.371 92	52.2 ± 8.1	3098.337 04	17.5 ± 9.8	4469.931 58	36.00 ± 2.0
4195.357 18	42.4 ± 2.9	3101.318 90	23.4 ± 9.2	4502.850 94	33.50 ± 2.0
4195.371 21	37.2 ± 2.7	3101.329 56	24.3 ± 8.7	4550.714 05	26.68 ± 2.0
4195.614 47	36.3 ± 3.3	3545.219 53	56.0 ± 7.2	4562.688 46	29.60 ± 2.0
4195.624 57	39.0 ± 4.9	3546.207 56	57.2 ± 5.8	5202.927 61	36.47 ± 2.0
4197.514 56	44.6 ± 2.8			5278.716 93	32.75 ± 2.0

This paper has been typeset from a TEX/LATEX file prepared by the author.